Suppression of transient beam-loading effects in storage rings via main-cavity power source feedforward scheme

PeiZhi Fang, Zhilong Pan, Yanqing Jia, Hongjuan Yao, Shuxin Zheng,* and Chuanxiang Tang
Department of Engineering Physics, Tsinghua University, Beijing, China

Xiujie Deng
Institute for Advanced Study, Tsinghua University, Beijing, China

(Received 23 June 2026; accepted 21 October 2026; published 5 November 2026)

Dual-frequency radio-frequency systems are widely deployed in high-brightness synchrotron radiation light sources to achieve electron bunch lengthening. However, the transient beam-loading (TBL) effect induced by bunch gaps causes significant synchronous phase shifts and severely compromises bunch-lengthening performance. To address this, we propose an active compensation scheme that suppresses voltage fluctuations in both the main and harmonic cavities by modulating only the driving voltage of the main cavity via a feedforward approach. To elucidate the underlying physical mechanisms, we establish a gap-induced linear decomposition analytical model, which decomposes the TBL-induced beam voltage into steady-state and transient components. Based on this model, we derive an optimization method to minimize power requirements, enabling the main-cavity TBL compensation to achieve performance levels comparable to those of broadband-cavity TBL compensation. The efficacy of this framework is demonstrated through two case studies: for an steady-state microbunching storage ring with a 7.5-MHz hardware half-bandwidth, the required single-cavity peak power is maintained at 158 kW, with normalized average radiation power improved from 78% to 97%; for the KEK light source storage ring with a 6-MHz bandwidth, the single-cavity peak power is optimized to 148 kW, successfully restoring the average bunch length from 31.1 to 40.9 ps. The proposed scheme establishes a highly efficient and cost-effective paradigm for TBL suppression, providing a promising technical pathway for next-generation light sources.

DOI: 10.1103/z3p2-lsz6

I. INTRODUCTION

Flattening the radio-frequency (rf) potential well with a harmonic cavity has become the baseline technique for high-brightness storage rings [1–4]. By diluting the longitudinal charge density of individual bunches, the method suppresses intrabeam scattering (IBS), extends the Touschek lifetime, and, through the enlarged synchrotron frequency spread, stabilizes the beam against longitudinal collective instabilities [1].

In practical storage ring operations, filling gaps are commonly employed to facilitate ion clearing and beam injection and extraction. However, when the gap duration becomes comparable to the cavity filling time, a strong transient beam-loading (TBL) effect is triggered [5]. This effect induces asymmetric fluctuations in the cavity voltage amplitude and phase along the bunch train, thereby undermining the conditions required for optimal bunch lengthening. Consequently, the majority of bunches deviate from their target longitudinal distribution, suffering from distribution distortion and centroid shifts that ultimately shorten the beam lifetime [5,6]. This issue is particularly critical for Steady-State Microbunching (SSMB) light sources, where the reliance on reversible microbunching necessitates precise synchronization between electron bunches and the seed laser. In this context, TBL-induced centroid shifts disrupt this delicate synchronization, leading to severe degradation in the coherence and intensity of the output radiation power [7].

Existing approaches for suppressing TBL include: (1) using cavities with low R/Q values to weaken beam-cavity interaction strength [3]; (2) adjusting the filling pattern by strategically placing "guard bunches" at the boundaries of the train to provide passive compensation for the missing load during the gap passage [8]. However, the former is limited by cavity design, as R/Q cannot be reduced indefinitely while maintaining high shunt impedance, and the latter is limited because high-charge bunches have short lifetimes, offering limited

*Contact author: zhengsx@tsinghua.edu.cn

Published by the American Physical Society under the terms of the Creative Commons Attribution 4.0 International license. Further distribution of this work must maintain attribution to the author(s) and the published article's title, journal citation, and DOI.

compensation. Therefore, active compensation based on feedforward control presents a more promising scheme: by compensating the cavity voltage via feedforward from the rf power source, voltage perturbations from TBL can theoretically be precisely canceled. However, feedforward schemes acting on the main and harmonic cavities usually impose high demands on generator power [3].

To circumvent the generator power bottleneck, alternative compensation strategies have been explored. One prominent approach is the dedicated broadband-cavity compensation feedforward (BCF) scheme, which effectively reduces transient power requirements while preserving compensation performance [9,10]. However, integrating such auxiliary cavities inevitably escalates engineering complexity, consumes scarce straight-section real estate, and introduces parasitic broadband impedance into the storage ring. Concurrently, following the Fourier-truncation feedforward approach pioneered at KEK [3,11,12], studies by the ALBA and BESSY collaboration investigated feedforward compensation applied directly to active harmonic cavities, demonstrating that truncating the Fourier series to a few dominant harmonics (e.g., $N = 2$) substantially lowers peak generator power demands [13,14]. Nonetheless, such direct Fourier truncation wastes the available system bandwidth: high truncation orders cannot be exploited, because the gibbs oscillations they introduce leave the compensated waveform plagued by ripple artifacts.

To address these limitations, this paper proposes a main-cavity feedforward (MCF) scheme that leverages the existing fundamental rf cavities to simultaneously mitigate transient voltage fluctuations across the entire dual-frequency system. Previous research has primarily treated the main and harmonic cavities independently; the absence of a unified theoretical optimization framework has reinforced the prevailing perception that feedforward compensation through the accelerating cavities demands prohibitively high peak power. To challenge this view, we formulate the gap-induced linear decomposition (GILD) model alongside a gap constraint relaxation (GCR) optimization algorithm to systematically identify global power minima. Our findings demonstrate that the proposed MCF framework achieves compensation flatness comparable to dedicated broadband-cavity solutions while keeping generator power requirements well within practical operational boundaries.

The remainder of this paper is organized as follows. Section II establishes the theoretical foundation by detailing the fundamentals of longitudinal dynamics and introducing the GILD model, along with its validity thresholds for high-Q cavities. Section III presents the architectural design of the proposed MCF scheme and derives analytical expressions to globally optimize cavity detuning and coupling factors under unconstrained bandwidth. To address practical hardware limitations, Sec. IV investigates parameter tuning under bandwidth constraints; it analyzes the detrimental impacts of the gibbs phenomenon and introduces a numerical optimization algorithm incorporating the GCR strategy. Section V validates the proposed framework through comprehensive case studies, performing parametric Pareto scans and numerical simulations for the SSMB and KEK light source (KEK-LS) storage ring scenarios. Section VI provides critical engineering insights by evaluating collective beam stability boundaries and benchmarking the MCF performance against broadband-cavity compensation schemes. Finally, Sec. VII summarizes the core findings and concluding remarks of this work.

II. ANALYTICAL MODELING OF TRANSIENT BEAM LOADING

A. Fundamentals of longitudinal dynamics

Consider a storage ring equipped with a double-rf system, where the main cavity is utilized to replenish the energy loss of the bunches, and the harmonic cavity is employed to achieve bunch lengthening. The total voltage of the system can be expressed as:

$$V_c(t) = \mathrm{Re}[\tilde{V}_{c,f}\exp(i\omega_{\mathrm{rf}}t) + \tilde{V}_{c,h}\exp(ih\omega_{\mathrm{rf}}t)], \quad (1)$$

where $\tilde{V}_{c,f}$ and $\tilde{V}_{c,h}$ are the complex voltage phasors of the main and harmonic cavities, respectively, and h is the frequency ratio of the harmonic cavity to the main rf system. These phasors can be explicitly written in terms of their amplitudes and phases as:

$$\tilde{V}_{c,f} = |\tilde{V}_{c,f}|\exp(i\phi_f), \qquad \tilde{V}_{c,h} = |\tilde{V}_{c,h}|\exp(i\phi_h), \quad (2)$$

where $|\tilde{V}_{c,f}|$ and $|\tilde{V}_{c,h}|$ denote the voltage amplitudes, while ϕ_f and ϕ_h represent the respective phases of the cavity voltages relative to the bunch.

Due to beam-loading effects, the cavity voltage should be the sum of the generator voltage and the beam-induced voltage. We assume that the harmonic cavity uses a passive scheme, so only the main cavity has a generator voltage term.

$$\tilde{V}_{c,f} = \tilde{V}_{g,f} + \tilde{V}_{b,f}, \qquad \tilde{V}_{c,h} = \tilde{V}_{b,h}, \quad (3)$$

where $\tilde{V}_{g,f}$ is the generator voltage for the main cavity and $\tilde{V}_{b,f}$ and $\tilde{V}_{b,h}$ are the beam-induced voltages for the main and harmonic cavities, respectively.

From the total voltage $V_c(t)$, the potential-well function $\Phi(t)$ can be derived, yielding the bunch density distribution $\rho(t)$:

$$\Phi(t) = -\frac{\alpha_c\omega_{\mathrm{rf}}}{2\pi h_0 E_0}\int_0^t \{e_0 V_c(t') - U_0\}dt', \quad (4)$$

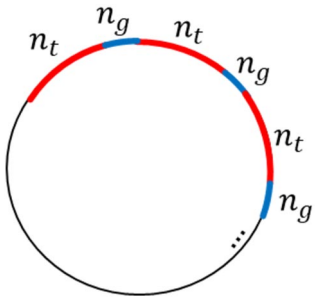


FIG. 1. Storage ring with n_t electron bunches with n_g empty bucket.

$$\rho(t) = \rho_0 \exp\left(-\frac{1}{\alpha_c^2 \sigma_\epsilon^2}\Phi(t)\right), \tag{5}$$

where α_c is the momentum compaction factor, h_0 is the harmonic number of the main cavity, E_0 is the beam energy, U_0 is the energy loss per turn due to synchrotron radiation, e_0 is the elementary charge, and σ_ϵ is the energy spread.

B. Analytical formulation of the gap-induced linear decomposition model

As shown in Fig. 1, in a storage ring containing multiple bunch trains, each structure consists of n_t buckets filled with electron bunches of charge q_b, followed by a gap of n_g empty buckets. Each bunch is assumed to have an identical longitudinal distribution, characterized by a bunch form factor F at the cavity resonant frequency. The time interval between consecutive buckets is t_b, and the total revolution period of the train-gap structure is $T = (n_t + n_g)t_b$.

The form factor is defined as the normalized bunch spectrum, $F \equiv \int_{-\infty}^{\infty} \rho_b(t) e^{-i\omega_{\rm res} t} \mathrm{d}t$, with $\int \rho_b(t)\mathrm{d}t = 1$, where $\rho_b(t)$ denotes the longitudinal charge distribution of a single bunch.

Under steady-state conditions, the beam-induced voltage $\tilde{V}_b$ is periodic with period T. Let $\tilde{V}_b^{(j)}$ denote the cavity voltage immediately preceding the j-th bunch in a train. The induced voltage for the first bunch, $\tilde{V}_b^{(1)}$, can be derived as follows [3]:

$$\begin{aligned}\tilde{V}_b^{(1)} &= -\frac{2k_n q_b F e^{n_g\alpha}}{1 - e^{(n_t+n_g)\alpha}} \sum_{l=1}^{n_t} e^{l\alpha} \\ &= -\frac{2k_n q_b e^{(n_g+1)\alpha}(1 - e^{n_t\alpha})}{(1 - e^{(n_t+n_g)\alpha})(1 - e^{\alpha})}.\end{aligned} \tag{6}$$

Here, $k_n = (\omega_{\rm res}/2)(R/Q)$ represents the cavity loss factor, while $\alpha = -(t_b/\tau_f)(1 - i\tan\psi)$ denotes the complex cavity decay factor per bucket time. Furthermore, $\tau_f = 2Q_L/\omega_{\rm res}$ is the cavity filling time and ψ is the detuning angle.

For a continuous-time description within the m-th train (where $m = 0, 1, 2, \ldots$ indexes the train number), let $t = mT + \tau$, with $\tau \in [0, T)$ being the intratrain time.

During beam passage ($0 < \tau \le n_t t_b$), corresponding to the j-th bunch where $j = \lceil \tau/t_b \rceil$:

$$\tilde{V}_b(\tau) = \tilde{V}_b^{(1)} e^{(\tau/t_b)\alpha} - 2k_n q_b F\, e^{(\tau/t_b - j + 1)\alpha} \sum_{l=0}^{j-1} e^{l\alpha}. \tag{7}$$

During gap passage ($n_t t_b < \tau \le T$), the voltage decays freely from its value at the end of the train:

$$\tilde{V}_b(\tau) = \left[\tilde{V}_b^{(1)} e^{n_t\alpha} - 2k_n q_b F \sum_{l=1}^{n_t} e^{l\alpha}\right] e^{(\tau/t_b - n_t)\alpha}. \tag{8}$$

In main and harmonic cavities, the loaded quality factor Q_L is typically designed to be high to minimize power consumption. Consider the high-Q_L regime where $|\alpha| \ll 1$: the exponential terms in Eqs. (7) and (8) can be simplified using a first-order Taylor expansion. By defining the average beam current as $I_0 = \frac{q_b}{t_b}\left(\frac{n_t}{n_t+n_g}\right)$, the beam-induced voltage can be linearized across the pulse and gap durations as follows:

During beam passage ($0 < \tau \le n_t t_b$):

$$\begin{aligned}\tilde{V}_b(\tau) &\approx -2k_n q_b F\left[\frac{n_g}{n_t+n_g}\frac{\tau - n_t t_b}{t_b} - \frac{n_t}{(n_t+n_g)\alpha}\right] \\ &= -(R/Q) I_0 F \frac{n_g}{n_t}\omega_{\rm res}(\tau - n_t t_b) - 2I_0 F \frac{R_L}{1 - i\tan\psi},\end{aligned} \tag{9}$$

and during gap passage ($n_t t_b < \tau \le (n_t + n_g)t_b$):

$$\begin{aligned}\tilde{V}_b(\tau) &\approx -2k_n q_b F\left[-\frac{n_t}{n_t+n_g}\frac{\tau - n_t t_b}{t_b} - \frac{n_t}{(n_t+n_g)\alpha}\right] \\ &= +(R/Q) I_0 F \omega_{\rm res}(\tau - n_t t_b) - 2I_0 F \frac{R_L}{1 - i\tan\psi}.\end{aligned} \tag{10}$$

Equations (9) and (10) can be decomposed into a time-independent steady-state component, $\tilde{V}_{b,\rm st}$, and a time-dependent transient component, $\tilde{V}_{b,\rm tr}(\tau)$:

$$\tilde{V}_b(\tau) = \tilde{V}_{b,\rm st} + \tilde{V}_{b,\rm tr}(\tau), \tag{11}$$

where $\tilde{V}_{b,\rm st} = -2I_0 F \frac{R_L}{1 - i\tan\psi}$ represents the steady beam loading, with $R_L = (R/Q)Q_L$ the loaded shunt impedance, ψ the cavity detuning angle [3], and $\tan\psi \equiv 2Q_L(\omega_{\rm res} - \omega_{\rm rf})/\omega_{\rm res}$. Here $\omega_{\rm rf} = h_0\omega_0$, with ω_0 the revolution angular frequency of the ring, is the drive frequency fixed by the beam: the main cavity must be driven at exactly $\omega_{\rm rf}$ and the harmonic cavity at $h\,\omega_{\rm rf}$. The cavity

resonant frequencies $\omega_{\mathrm{res},f}$ and $\omega_{\mathrm{res},h}$, in contrast, are free parameters adjusted through detuning. This decoupling of the linear transient slope from the static component forms the basis of the GILD model. Consequently, the transient term $\tilde{V}_{b,\mathrm{tr}}(\tau)$ is given by:

$$\tilde{V}_{b,\mathrm{tr}}(\tau)=\begin{cases}-(R/Q)I_0F\frac{n_g}{n_t}\omega_{\mathrm{res}}(\tau-n_tt_b), & 0<\tau\le n_tt_b\\ +(R/Q)I_0F\omega_{\mathrm{res}}(\tau-n_tt_b). & n_tt_b<\tau\le T\end{cases}. \tag{12}$$

Notably, this transient voltage manifests as a triangular waveform. Its peak amplitude scales linearly with the cavity geometric shunt impedance (R/Q), the resonant frequency ω_{res}, and the average beam current I_0. This explicit dependence physically justifies the preference for low-R/Q cavity designs [3] and explains why TBL effects are inherently more pronounced in harmonic cavities and high-current storage rings. Given that the form factor F typically approaches unity, this linear fluctuation directly accounts for the synchronous phase shifts documented in previous studies [3,4,6,15], while providing a physical explanation for why compensating for the imaginary part of the transient voltage yields negligible benefits [9].

Beyond its mathematical formulation, the GILD model offers significant engineering utility. Although strictly derived under the assumption of uniformly distributed gaps, the model provides an elegant and intuitive analytical framework that captures the essence of beam-induced voltage fluctuations. By distilling the complex, time-domain TBL-induced beam voltage into a simple, closed-form linear representation, the GILD model enables rapid estimation of beam-loading effects without the need for extensive numerical simulations. This capability is particularly advantageous for theoretical investigations into feedforward compensation strategies, where quick design iterations and sensitivity analyses are required to optimize system parameters for effective TBL suppression.

Finally, it is worth noting that the GILD model assumes uniform bunch spacing and a constant form factor. While the TBL-induced synchronous phase shift in an uncompensated ring technically renders this constant-t_b assumption nonself-consistent, the primary objective of the proposed feedforward scheme is to suppress these fluctuations and restore a uniform longitudinal profile. Therefore, utilizing the GILD-derived voltage as the feedforward compensation signal is not only mathematically valid but also physically self-consistent for the targeted corrected state.

C. Benchmarking and validity of the high-Q approximation

A fundamental premise of the proposed GILD model relies on the high-quality-factor cavity approximation. To validate the proposed GILD model under different quality-factor conditions, we conducted a detailed comparison between the semianalytical solution, evaluated directly from Eqs. (7) and (8), and the linearized analytical GILD solution [based on Eqs. (9) and (10)]. The loaded quality factor Q_L was varied over 3 orders of magnitude, specifically taking values of 10^2, 10^3, and 5×10^3, while other parameters were fixed: $n_t=450$ bunches per train, $n_g=50$ empty buckets, $I_0=0.1$ A, $\omega_{rf}=500$ MHz, $R/Q=50\ \Omega$, and $\tan\psi=0.5$.

To quantify the validity regime of the model, we introduce the parameter χ, defined as the ratio of the bunch-train duration to the cavity filling time:

$$\chi\equiv\frac{n_tt_b}{\tau_f}\sqrt{1+\tan^2\psi}=\frac{n_tt_b}{\tau_f}|\sec\psi|, \tag{13}$$

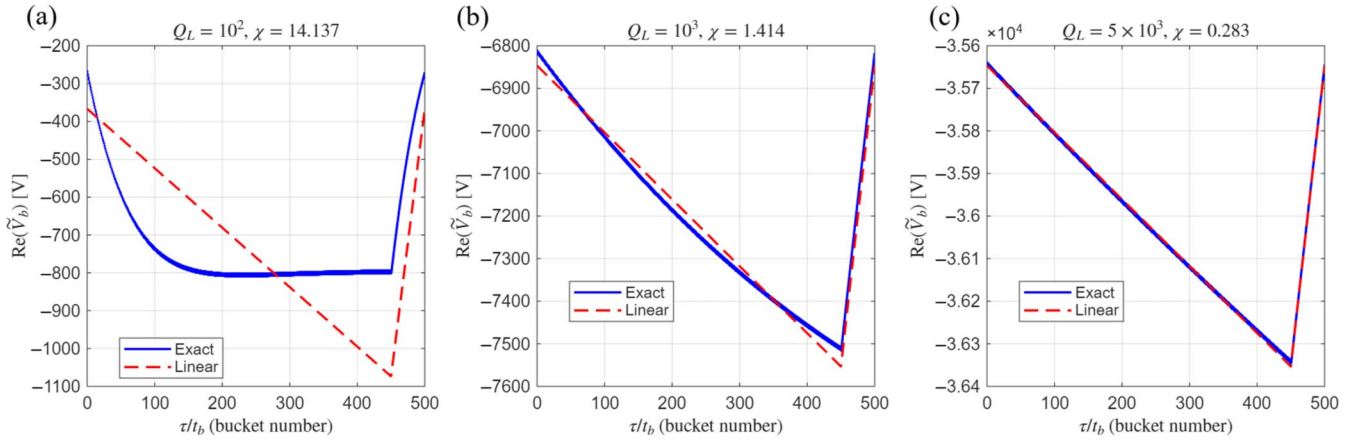


FIG. 2. Comparison of the beam-induced voltage waveforms obtained from the semianalytical solution of Eqs. (7) and (8) (solid blue) and the GILD model (dashed red) for three different loaded quality factors: (a) $Q_L=10^2$ ($\chi=14.137$), (b) $Q_L=10^3$ ($\chi=1.414$), and (c) $Q_L=5\times10^3$ ($\chi=0.283$). The saturation parameter χ determines the validity of the linear approximation, with good agreement achieved for $\chi<1$.

where $\tau_f = 2Q_L/\omega_{\rm res}$ is the cavity filling time. This dimensionless parameter characterizes the degree of cavity voltage decay during the beam passage.

Figure 2 compares the semianalytical and linearized beam-induced voltage waveforms across different regimes defined by χ. The former is evaluated directly from Eqs. (7) and (8) without further simplification, so that the full exponential decay and accumulation of the cavity field from bunch to bunch are retained. The results demonstrate that the GILD model remains highly accurate for $\chi < 1$ (e.g., $Q_L = 5 \times 10^3$), where the bunch-train duration is shorter than the cavity filling time. As χ increases toward and beyond unity (e.g., $Q_L \leq 10^3$), the cavity voltage approaches saturation, leading to a monotonic increase in the discrepancy between the GILD approximation and the semianalytical solution. Consequently, $\chi < 1$ is established as the fundamental criterion for the validity of the GILD analytical model.

III. MAIN-CAVITY FEEDFORWARD SCHEME AND POWER OPTIMIZATION

A. Architecture of the MCF scheme

The objective of the MCF scheme is to modulate the main-cavity generator voltage $\tilde{V}_{g,f}$ to dynamically cancel the transient terms originating from both the main and passive harmonic cavities.

Ideally, to achieve optimal bunch lengthening (the "flat-potential" condition), the total accelerating voltage V_c must satisfy the following three conditions simultaneously at the synchronous phase:

$$V_c(0) = U_0, \qquad V_c'(0) = 0, \qquad V_c''(0) = 0. \tag{14}$$

However, it is important to note that in the main-cavity feedforward setup, the first and third conditions in Eq. (14) are inherently contradictory. Since the harmonic cavity operates passively, its second-order derivative contribution (V_c'') cannot be independently modulated at the h-th harmonic frequency. Consequently, the MCF scheme can only satisfy the voltage value and its first derivative, leading to a "near-flat" potential well [16] rather than a perfectly flat potential well throughout the entire bunch train.

As shown in Eqs. (1) and (3), the total accelerating voltage is the superposition of the generator and beam-induced components. By requiring the total voltage to remain constant, the compensation requirements for the main-cavity generator voltage are determined by:

$$\mathrm{Re}(\tilde{V}_{g,f}) = U_0 - \mathrm{Re}(\tilde{V}_{b,f} + \tilde{V}_{b,h}), \tag{15}$$

$$\mathrm{Im}(\tilde{V}_{g,f}) = -\mathrm{Im}(\tilde{V}_{b,f} + \tilde{V}_{b,h}). \tag{16}$$

By substituting the analytical expressions of the GILD model into Eqs. (15) and (16), we derive the explicit time-dependent generator voltage. For the beam-passage duration ($0 < \tau \leq n_t t_b$), the required main-cavity generator voltage is

$$\tilde{V}_{g,f}(\tau) = \underbrace{\tilde{V}_{c,f} + 2I_0F_f\frac{R_{L,f}}{1 - i\tan\psi_f}}_{\tilde{V}_{g,f,\mathrm{st}}} \underbrace{+(R/Q)_{\rm tot}I_0\frac{n_g}{n_t}\omega_{rf}\tau}_{\tilde{V}_{g,f,\mathrm{tr}}(\tau)}, \tag{17}$$

and during the gap passage ($n_t t_b < \tau \leq (n_t + n_g)t_b$), it follows

$$\tilde{V}_{g,f}(\tau) = \underbrace{\tilde{V}_{c,f} + 2I_0F_f\frac{R_{L,f}}{1 - i\tan\psi_f}}_{\tilde{V}_{g,f,\mathrm{st}}} \underbrace{-(R/Q)_{\rm tot}I_0\omega_{rf}\tau}_{\tilde{V}_{g,f,\mathrm{tr}}(\tau)}. \tag{18}$$

To simplify the notation, we define the total effective $(R/Q)_{\rm tot}$ as:

$$(R/Q)_{\rm tot} = F_f(R/Q)_f + hF_h(R/Q)_h. \tag{19}$$

Here F_f and F_h denote the bunch form factors evaluated at the resonant frequencies of the main and harmonic cavities, respectively. Since the harmonic cavity operates at the h-th harmonic frequency ($\omega_h = h\omega_{\rm rf}$), it induces a voltage transient slope that is h times steeper than that of the main cavity for a given R/Q value.

The steady-state terms in Eqs. (17) and (18) provide the nominal cavity voltage $\tilde{V}_{c,f}$ required for acceleration while compensating the steady beam-loading effect. The transient term provides a linear voltage ramp that simultaneously counteracts the transient variation of both the main and harmonic cavities.

To evaluate the power demands on the rf generator for the MCF scheme, we start from the beam-cavity interaction equation [17,18] and establish the relationship between the required generator voltage $\tilde{V}_{g,f}(t)$ and the drive current $\tilde{I}_{g,f}(t)$:

$$\frac{d\tilde{V}_{g,f}}{dt} + \frac{\omega_{\mathrm{res},f}}{2Q_{L,f}}(1 - i\tan\psi_f)\tilde{V}_{g,f} = \omega_{\mathrm{res},f}\left(\frac{R}{Q}\right)_f\tilde{I}_{g,f}. \tag{20}$$

Rearranging Eq. (20) to solve for the required generator current yields

$$\tilde{I}_{g,f}(t) = \frac{1}{\omega_{\mathrm{res},f}(R/Q)_f}\frac{d\tilde{V}_{g,f}}{dt} + \frac{1 - i\tan\psi_f}{2Q_{L,f}(R/Q)_f}\tilde{V}_{g,f}(t). \tag{21}$$

The generator power demand $P_{g,f}$ is determined by the generator current [17,18]; the equation is by:

$$P_{g,f}(t) = \frac{1}{2}\frac{R_f}{\beta_f}|\tilde{I}_{g,f}(t)|^2 = \frac{1}{2}(R/Q)_f\frac{Q_0 Q_L}{Q_0 - Q_L}|\tilde{I}_{g,f}(t)|^2, \quad (22)$$

where R_f is the main-cavity shunt impedance, β_f is the main-cavity coupling coefficient, and Q_0 is the intrinsic quality factor of the main cavity.

The analytical decomposition of the generator current in Eq. (21) yields significant physical insights into the power demand of the feedforward. The required generator voltage $\tilde{V}_{g,f}$ comprises a steady-state term and a transient linear ramp term. The derivative of this transient ramp, $d\tilde{V}_{g,f}/dt$, represents the reactive current necessitated by the rapid slewing of the cavity field. This term is the primary driver of the peak power surge, reflecting a scenario in which the transmitter power is predominantly consumed in contending with the electromagnetic inertia of the cavity's stored energy.

A critical observation is the contrasting dependency of these two components on the cavity quality factor Q_L. While the current required for transient compensation is independent of Q_L, the associated peak power scales linearly with Q_L. Consequently, lowering the Q factor (increasing bandwidth) effectively mitigates the power demands of transient compensation—a principle that justifies the use of a broadband cavity. However, such a reduction in Q_L simultaneously increases the steady-state power demand.

B. Analytical optimization of the power demand

To minimize the rf power penalty imposed by the active feedforward scheme, this section derives the optimal cavity-design parameters—specifically, the loaded quality factor (Q_L) and the detuning angular frequency ($\Delta\omega$).

Under the practical condition where the steady-state voltage dictates the overall amplitude ($|\tilde{V}_{g,f,\mathrm{st}}| \gg |\tilde{V}_{g,f,\mathrm{tr}}|$) and $F_f = 1$, we can approximate the term proportional to $\tilde{V}_{g,f}$ in Eq. (21) using the steady-state component $\tilde{V}_{g,f,\mathrm{st}}$ solely. This simplification yields explicit analytical expressions for the required generator current in two distinct temporal regions:

During the beam passage ($0 < \tau \le n_t t_b$):

$$\tilde{I}_{g,f,\mathrm{beam}} \approx \frac{(R/Q)_{\mathrm{tot}}}{(R/Q)_f} I_0 \frac{n_g}{n_t} + \frac{1 - i\tan\psi_f}{2R_{L,f}}\tilde{V}_{c,f} + I_0. \quad (23)$$

During the gap passage ($n_t t_b < \tau \le (n_t + n_g)t_b$):

$$\tilde{I}_{g,f,\mathrm{gap}} \approx -\frac{(R/Q)_{\mathrm{tot}}}{(R/Q)_f} I_0 + \frac{1 - i\tan\psi_f}{2R_{L,f}}\tilde{V}_{c,f} + I_0. \quad (24)$$

The minimization of the power demand inherently formulates a minimax optimization problem. The global minimum is achieved when the required generator power is dynamically balanced between the beam and gap passages:

$$|\tilde{I}_{g,f,\mathrm{beam}}| = |\tilde{I}_{g,f,\mathrm{gap}}|. \quad (25)$$

Since $P_{g,f} \propto |\tilde{I}_{g,f}|^2$, the peak power over one filling period is set by the larger of the two passage currents in Eqs. (23) and (24). With the detuning ψ_f providing the only free phase, this peak is minimized when the two current magnitudes are equal, in analogy with the balanced beam-loading operation of singly detuned rf systems [19,20].

By applying this equal-amplitude condition at the temporal boundaries, the optimal detuning angular frequency for the main cavity is analytically derived as:

$$\Delta\omega_{f,\mathrm{opt}} = -\omega_{\mathrm{res},f}\frac{\kappa(R/Q)_f Q_L I_0 + V_{c,f}\cos\phi_f}{2V_{c,f}\sin\phi_f Q_L}, \quad (26)$$

where $\kappa = \frac{2n_t - (n_t - n_g)(R/Q)_{\mathrm{tot}}/(R/Q)_f}{n_t}$ is introduced for brevity.

To physically elucidate the essence of these matching conditions, it is highly instructive to decompose the driving forces into three distinct equivalent current components: the active intrinsic wall-loss current $I_c = V_{c,f}/[(R/Q)_f Q_0]$, the active steady-state beam-loading current $I_{\mathrm{st}} = \kappa I_0 \cos\phi_f$, and the reactive transient-compensation current $I_{\mathrm{tr}} = [(R/Q)_{\mathrm{tot}}/(R/Q)_f]I_0 \sin\phi_f$.

Finally, by substituting the optimal detuning condition and differentiating the power expression with respect to Q_L, the optimal loaded quality factor that globally minimizes the total power consumption is obtained analytically:

$$Q_{L,\mathrm{opt}} = \frac{Q_0}{1 + \frac{\sqrt{(I_{\mathrm{st}} + I_c)^2 + I_{\mathrm{tr}}^2}}{I_c}}. \quad (27)$$

Recalling the relation $Q_L = Q_0/(1+\beta)$ between the loaded quality factor and the coupling coefficient reveals the optimal coupling factor:

$$\beta_{f,\mathrm{opt}} = \frac{\sqrt{(I_{\mathrm{st}} + I_c)^2 + I_{\mathrm{tr}}^2}}{I_c}. \quad (28)$$

Substituting $Q_{L,\mathrm{opt}}$ back yields the absolute minimum power requirement P_{opt} for optimum feedforward compensation:

$$P_{\mathrm{opt}} = \frac{V_{c,f}}{4\sin^2\phi_f}\left[\sqrt{(I_{\mathrm{st}} + I_c)^2 + I_{\mathrm{tr}}^2} + (I_{\mathrm{st}} + I_c)\right]. \quad (29)$$

To appreciate the universality of this formulation, it is highly instructive to examine the degenerate case of a single rf system, where harmonic cavities are absent (i.e., $(R/Q)_{\mathrm{tot}} = (R/Q)_f$). Under this condition, assuming a

cavity voltage phase of $\phi_f = \pi/2$ (corresponding to a purely reactive beam with zero net acceleration), the optimal cavity parameters derived from the GILD model naturally degenerate to the half-detuning scheme widely employed at CERN [19,20].

IV. FEEDFORWARD OPTIMIZATION UNDER BAND-LIMITED CONSTRAINTS

In the preceding section, the optimal feedforward parameters and power requirements were derived under the implicit assumption of infinite system bandwidth. In practical rf systems, however, the solid-state amplifiers and the associated low-level rf (LLrf) control loops possess finite bandwidths. To address this physical constraint, this section investigates the feedforward parameter optimization under band-limited conditions.

A. Fourier series truncation and the associated gibbs phenomenon

We first evaluate the Fourier series truncation method, previously explored at the KEK-LS [3]. From a signal-processing perspective, Parseval's theorem ensures that a truncated Fourier series minimizes the mean-square error between the synthesized waveform and the ideal waveform within a given bandwidth.

A critical challenge emerges when evaluating the reactive generator current I_g. As indicated by the cavity dynamics in Eq. (21), I_g is primarily determined by the time derivative of the transient voltage $\tilde{V}_{\mathrm{tr}}(\tau)$. Given that $\tilde{V}_{\mathrm{tr}}(\tau)$ exhibits a triangular profile, its derivative is fundamentally a square wave characterized by abrupt jump discontinuities at the bunch-train boundaries. When this derivative is synthesized via a truncated Fourier series, the gibbs phenomenon inevitably arises. Instead of converging uniformly, the series produces persistent oscillatory ringing—the gibbs artifacts—in the immediate vicinity of these discontinuities. These artifacts manifest as high-frequency overshoot in the required generator current I_g, thereby necessitating an increased peak generator power to accommodate the stringent transient voltage requirements.

To analytically quantify the impact of the gibbs phenomenon on the required generator current, we define the derivative factor $k(\tau)$ as the ratio of the derivative of synthesized waveform $\mathcal{D}(\tau)$ to the slope factor S_0:

$$k(\tau) = \frac{\mathcal{D}(\tau)}{S_0}, \tag{30}$$

where S_0 represents the physical slope factor required for exact transient compensation. This value is determined solely by the bunch-train filling pattern and the compensation amplitude:

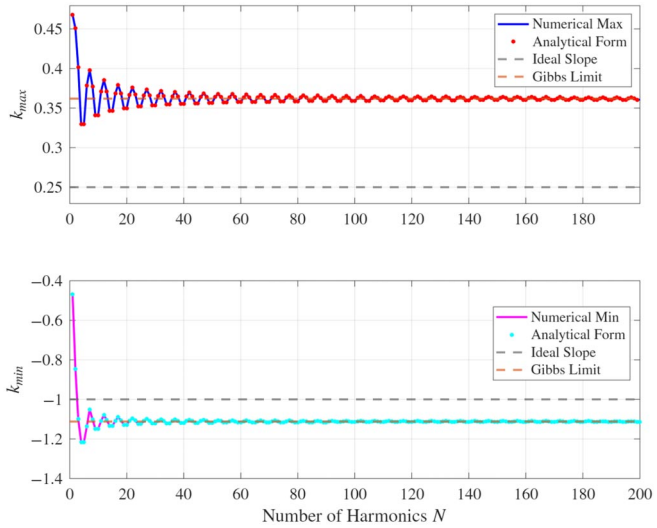


FIG. 3. Convergence of the normalized derivative factors $k_{\max}$ and $k_{\min}$ of the Fourier-truncated waveform as a function of the number of harmonics N ($d = 0.8$; the corresponding ideal values are $k_{\max} = 0.25$ and $k_{\min} = -1$). The orange dashed lines represent the gibbs limits, and the dark gray dashed lines show the ideal slope values.

$$S_0 = \frac{A}{T(1-d)}. \tag{31}$$

Here, A represents the peak-to-peak amplitude of the triangular voltage waveform, and $d = n_t/(n_t + n_g)$ denotes the duty cycle of the bunch train. Equivalently, $S_0 = \omega_{\mathrm{rf}}(R/Q)_{\mathrm{tot}} I_0$, i.e., the gap-passage slope magnitude of the ideal compensation ramp of Eqs. (17) and (18). The derivative factor $k(\tau)$ is therefore the instantaneous slew rate of the synthesized generator voltage, normalized to this ideal gap slope: perfect infinite-bandwidth compensation corresponds to $k = (1-d)/d\,(= n_g/n_t)$ during the beam passage and $k = -1$ during the gap.

As illustrated in Fig. 3, the maximum and minimum derivative factors $k_{\max}$ and $k_{\min}$ are, respectively, the largest and smallest values attained by the synthesized $k(\tau)$ over one filling period—for a duty cycle of $d = 0.8$, the ideal values are $k_{\max} = (1-d)/d = 0.25$ and $k_{\min} = -1$. Because the peak generator power is dictated by the worst-case (largest-magnitude) generator current rather than by its time average, it is precisely these two extrema that control the required transmitter power; this is why $k_{\max}$ and $k_{\min}$, rather than the full profile $k(\tau)$, appear in the current and power expressions of Eqs. (32)–(35) below. These results clearly demonstrate the nonuniform convergence characteristic of the gibbs phenomenon [21]: as the harmonic order N increases, the $k_{\max}$ and $k_{\min}$ fail to converge to the ideal slope near the temporal discontinuities. Instead, they exhibit persistent oscillatory ringing, with the peak magnitudes asymptotically stabilizing at the gibbs limits, which are approximately 1.089 times the ideal

value, a direct consequence of the square-wave nature of the time derivative of the triangular target waveform.

By incorporating the derivative factors $k_{\max}$ and $k_{\min}$ into the generator current, the current during the beam and gap passages can be expressed as:

$$\tilde{I}_{g,f,\mathrm{beam}} = \frac{(R/Q)_{\mathrm{tot}}}{(R/Q)_f} I_0 k_{\max} + \frac{1 - i\tan\psi_f}{2R_{L,f}} \tilde{V}_{c,f} + I_0, \quad (32)$$

$$\tilde{I}_{g,f,\mathrm{gap}} = \frac{(R/Q)_{\mathrm{tot}}}{(R/Q)_f} I_0 k_{\min} + \frac{1 - i\tan\psi_f}{2R_{L,f}} \tilde{V}_{c,f} + I_0. \quad (33)$$

To facilitate a concise analytical solution, we define the bandwidth-dependent factors H_Σ and H_Δ:

$$H_\Sigma = \frac{(R/Q)_{\mathrm{tot}}}{(R/Q)_f}(k_{\max} + k_{\min}),$$
$$H_\Delta = \frac{(R/Q)_{\mathrm{tot}}}{(R/Q)_f}(k_{\max} - k_{\min}). \quad (34)$$

The optimal parameters—specifically the detuning $\Delta\omega_{f,\mathrm{opt}}$, the loaded quality factor $Q_{L,\mathrm{opt}}$, and the minimum power P_{opt}—preserve the exact analytical structures of Eqs. (26)–(29). The extension to band-limited tracking is seamlessly achieved by mapping the intermediate driving terms to their generalized counterparts: the reactive transient-compensation current is updated to $I_{\mathrm{tr}} = H_\Delta I_0 \sin\phi_f$, and the effective geometric coefficient is replaced by $\kappa = H_\Sigma + 2$. Consequently, the bandwidth-dependent distortion factors are directly embedded into the optimization framework.

Under the assumption that steady-state loading and cavity wall losses are negligible ($I_{\mathrm{st}} \approx 0, I_c \approx 0$), the minimum forward power P_{opt} under finite-bandwidth constraints simplifies to:

$$P_{\mathrm{opt}} \approx \frac{1}{4}\frac{V_{c,f} I_0}{\sin\phi_f}\frac{(R/Q)_{\mathrm{tot}}}{(R/Q)_f}(k_{\max} - k_{\min}). \quad (35)$$

Equation (35) explicitly reveals that the optimal rf power scales linearly with the magnitude $(k_{\max} - k_{\min})$. As N continues to rise, the term $(k_{\max} - k_{\min})$ oscillates and asymptotically stabilizes at the gibbs limit, leading to a nonvanishing power overhead that is approximately 18.7% higher than the ideal infinite-bandwidth prediction.

B. Numerical optimization via gap constraint relaxation

As shown in the previous section, although a finite Fourier series effectively minimizes the global fitting error, it inevitably triggers the gibbs phenomenon at the sharp boundaries of the bunch train. These characteristic overshoots artificially inflate the factor $k_{\max}$ and $k_{\min}$. Because the required rf power is strictly dictated by these peak factors, the gibbs-induced overshoots severely escalate the power demand, imposing a heavy penalty on the rf power source requirements.

To bypass the inherent limitations of analytical Fourier truncation, a numerical optimization approach is proposed. Instead of relying on fixed analytical Fourier coefficients, the transient generator voltage waveform $V_{\mathrm{opt},g,\mathrm{tr}}(\tau)$ is parameterized using a finite harmonic expansion:

$$V_{\mathrm{opt},g,\mathrm{tr}}(\tau) = \sum_{n=1}^{N}[a_n \cos(n\omega\tau) + b_n \sin(n\omega\tau)], \quad (36)$$

where $\mathbf{c} = \{a_1, b_1, \cdots, a_N, b_N\}$ denotes the vector of $2N$ tunable coefficients. To quantify the performance of this optimized waveform, we evaluate the derivative factor $k(\tau)$, defined in Eq. (30), as the ratio of the synthesized slope to the slope factor S_0:

$$k(\tau) = \frac{1}{S_0}\frac{dV_{g,f}(\tau)}{d\tau} = \frac{t_b}{2\pi(R/Q)_{\mathrm{tot}} I_0}\frac{dV_{\mathrm{opt},g,\mathrm{tr}}(\tau)}{d\tau}. \quad (37)$$

The physical justification for this optimization relies on the operational asymmetry of the storage ring. Strict fidelity of the cavity voltage is mandatory only during the beam passage (T_{beam}). Conversely, the voltage within the beam gap (T_{gap}) is physically inconsequential to the beam dynamics, provided the boundary conditions align smoothly with the head and tail of the bunch train. By exploiting this physical characteristic, the fitting constraints within T_{gap} are deliberately relaxed. This allows the optimizer the geometric freedom to "round-off" transitions and actively suppress gibbs overshoots. This strategy is formally designated as GCR.

To systematically search for the optimal harmonic coefficients $\mathbf{c}$ under the GCR framework, we construct a composite objective function $\mathcal{J}$ that balances power efficiency against compensation fidelity:

$$\mathcal{J}(\mathbf{c}) = w_P P_{\mathrm{opt}}(k_{\max}, k_{\min}) + w_E \int_{T_{\mathrm{beam}}} |V_{\mathrm{opt},g,\mathrm{tr}}(\tau) - V_{g,f,\mathrm{tr}}(\tau)|^2 \, \mathrm{d}\tau, \quad (38)$$

where the optimization balance is governed by the weighting factors w_P and w_E. A dominant w_P prioritizes peak power suppression by smoothing the transitions at the gap boundaries, while a higher w_E emphasizes waveform fidelity to ensure precise beam-loading compensation. By tuning the ratio $C \propto w_E/w_P$, the algorithm can be flexibly tailored to specific operational requirements.

Finally, to minimize this nonlinear objective function, we employ the Sequential Quadratic Programming (SQP) algorithm [22,23]. SQP is particularly well suited for this application, as it effectively handles nonlinear trade-offs

by iteratively solving quadratic approximations of the Lagrangian function. This iterative refinement ensures that the optimizer converges robustly to a local minimum, yielding the optimal harmonic coefficients that satisfy both the transmitter load limits and the beam-on voltage requirements.

V. NUMERICAL RESULTS AND CASE STUDIES

To validate the proposed MCF scheme and the GCR-based optimization algorithm, this section provides a comprehensive numerical analysis spanning two distinct operational scenarios: a KEK-LS storage ring case evaluating bunch-length variations and an SSMB storage ring case assessing perturbation-induced radiation power degradation. Despite the differing underlying physics and optimization objectives, the TBL effects are successfully counteracted via the MCF compensation scheme in both machines.

A. Application to KEK-LS: Impact on bunch-length dynamics

To quantitatively demonstrate the optimization performance of the proposed GCR strategy, a detailed case study is performed based on the design parameters of the KEK-LS storage ring. The nominal machine specifications and the corresponding double-rf system baseline configuration are systematically summarized in Tables I and II, respectively.

According to the GILD model, the TBL effects induced by the asymmetric filling pattern generate a triangular transient voltage $V_{b,\mathrm{tr}}$. This transient voltage heavily distorts the potential well, resulting in significant synchronous phase shifts and shortening the bunch length. To counteract this distortion, the proposed MCF scheme employs a GCR-based optimization algorithm to synthesize a corrective voltage profile that actively compensates for the TBL-induced transient. To establish an intuitive understanding of this compensation mechanism, Fig. 4 illustrates a grid comparison of the optimized, synthesized profiles—specifically the normalized derivative factor $k(\tau)$ and the corresponding normalized compensation voltage waveform—under a low-bandwidth scenario ($N = 4$) and a high-bandwidth scenario ($N = 20$) across different weighting parameters C (where $C \propto w_E/w_P$).

TABLE I. Principal parameters of the KEK-LS.

Parameter	Symbol	Value
Nominal beam energy	E_0	3.0 GeV
Stored beam current	I_0	500 mA
Radio frequency (fundamental)	f_{rf}	500.07 MHz
Harmonic number	h_0	952
Synchrotron radiation loss per turn	U_0	851 keV
Main rf voltage	$V_{c,f}$	2.5 MV
Natural relative energy spread (rms)	σ_ϵ	7.3×10^{-4}
Momentum compaction factor	α_c	2.2×10^{-4}
Filling patterns	$\cdots$	$2 \times (446b + 30e)$

TABLE II. Principal parameters of the double-rf system for the KEK-LS at the beam current of 500 mA.

Parameter	Symbol	Main rf ($n = 1$)	Harmonic rf ($n = 3$)
Rf voltage	$V_{c,n}$	2.5 MV	777 kV
Synchronous phase	$n\phi_n$	1.178 rad	−1.708 rad
Tuning angle	ψ_n	−0.962 rad	1.433 rad
Total R/Q	R_n/Q	437.5 Ω	193 Ω
Total shunt impedance	R_n	17.5 MΩ	7.24 MΩ
Cavity coupling coefficient	β_n	3.5	0.27
Cavity detuning amount	$\Delta f_{\mathrm{res},n}$	−40.3 kHz	185 kHz

As observed in the low-bandwidth regime ($N = 4$), the system suffers from severe spectral scarcity, necessitating a strict compromise. When power minimization is heavily penalized (small C), the tracking profiles at the bunch-train boundaries are significantly rounded off, implying that the unconstrained beam gap acts as a temporal buffer to redistribute the local slope and clip generator power overhead. Conversely, when tracking fidelity dominates (large C), the waveform is forced to match the discontinuous target, reintroducing severe gibbs overshoots and high-frequency ringing.

A qualitative transition occurs when expanding the harmonic bandwidth to $N = 20$. As shown in the lower row of Fig. 4, even under the stringent tracking constraint

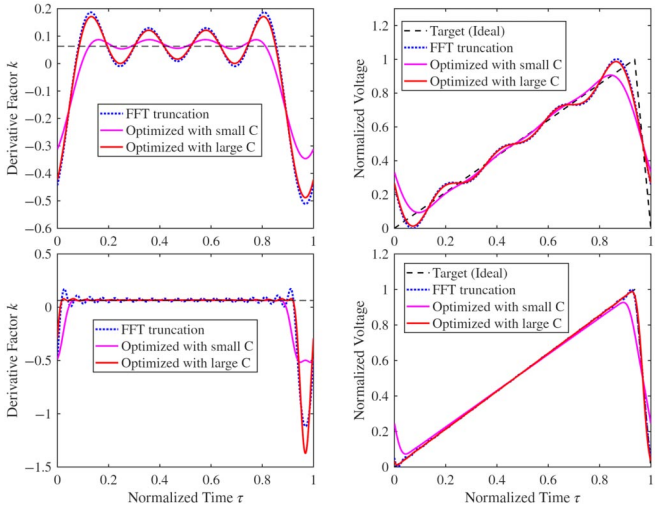


FIG. 4. Comparison of the derivative factor $k(\tau)$ (left column) and normalized voltage waveforms $V(\tau)/S_0$ (right column) for $N = 4$ (top row) and $N = 20$ (bottom row). The dashed curves represent the ideal target, the dotted curves denote the analytical Fourier truncation, and the solid lines show the optimized profiles synthesized under small C and large C (where $C \propto w_E/w_P$).

(large C), the optimized solution eliminates gibbs-induced distortions while maintaining high-precision tracking within the beam-on region. This behavior is fundamentally governed by the enhanced temporal resolution of higher harmonics. From signal-processing principles, the minimum rise time for a band-limited step transition scales as $\tau_r \approx T/(2N)$. Since the normalized gap duration is $\Delta\tau_g = (1-d)T$, confining a full transient cycle (a rapid fall and rise) strictly within the nonbeam interval requires $2\tau_r < \Delta\tau_g$. This yields a fundamental bandwidth-gap compatibility criterion for the critical harmonic threshold N_c:

$$N > N_c = \frac{1}{1-d}. \tag{39}$$

For the KEK-LS fill pattern, $N_c \approx 15.9$. Below this threshold ($N < N_c$), the transient response is geometrically choked by the narrow beam gap, forcing the aforementioned compromise between boundary smoothing and tracking fidelity. In the spectral abundance regime ($N > N_c$), the response becomes rapid enough to fully confine the corrective oscillations for gibbs suppression within the $\Delta\tau_g$ buffer, thereby completely decoupling the power suppression mechanism from the active beam-compensation precision.

To systematically map this trade-off between the single-cavity peak rf power (P_{cav}) and the tracking accuracy across all operational regimes, a global Pareto optimization frontier is generated by continuously scanning the weighting ratio C. To quantitatively evaluate the optimization algorithm's ability to synthesize the desired voltage profile, we employ the relative root-mean-square error (ϵ_{rel}) as the primary performance metric, defined as:

$$\epsilon_{\mathrm{rel}} = \sqrt{\frac{\sum_{i=1}^{M}(V_{\mathrm{opt},i} - V_{\mathrm{target},i})^2}{\sum_{i=1}^{M} V_{\mathrm{target},i}^2}} \times 100\%, \tag{40}$$

where $V_{\mathrm{opt},i}$ and $V_{\mathrm{target},i}$ correspond to the voltages sampled at the i-th filled bucket of the optimized and target voltage vectors, respectively, and M denotes the total number of filled buckets.

The resulting Pareto optimal curves across various harmonic limits N are illustrated in Fig. 5, with the analytical Fourier series truncation solutions serving as baselines.

The Pareto frontiers visually corroborate the N_c threshold criterion. For $N < N_c$, the optimized frontiers strictly converge toward their respective Fourier-truncation baselines (marked by $\times$) due to the structural lack of geometric freedom within the beam gap. Conversely, for $N > N_c$, the Pareto curves decisively detach from these analytical markers and shift toward the lower-left region of the objective space. This displacement represents a strict Pareto improvement, demonstrating that the GCR strategy

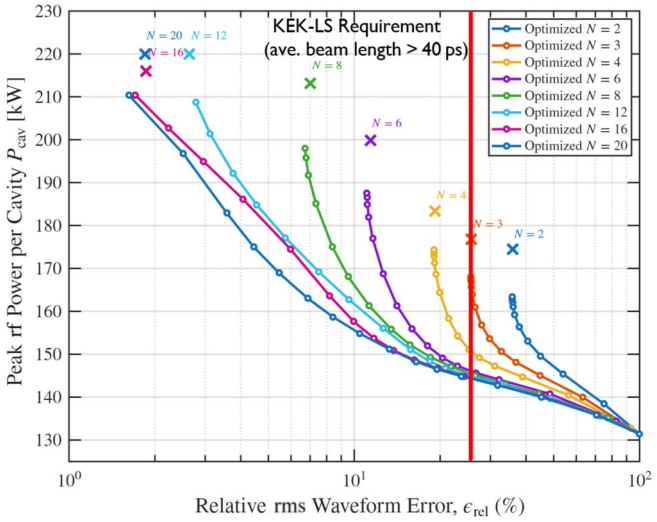


FIG. 5. Pareto optimization frontiers mapping the single-cavity peak rf power P_{cav} against the relative tracking error ϵ_{rel} for different harmonic bandwidths N. The markers ($\times$) indicate the unoptimized analytical Fourier series truncation solutions.

successfully circumvents classical Fourier synthesis limits to simultaneously achieve minimized power consumption and superior beam-passage voltage tracking.

From an engineering perspective, while operating at the spectral abundance regime ($N > N_c$) yields near-ideal flat-potential compensation, implementing such high-order harmonic systems imposes severe hardware complexity and bandwidth constraints on the rf cavities and power amplifiers. A more practical design strategy relies on exploiting the distinct "knee" (the region of maximum curvature) present on the Pareto curves at moderate bandwidths ($N < N_c$). Operating near this knee allows for a substantial reduction in peak power demand at the expense of a marginal, well-controlled degradation in compensation precision.

To anchor this threshold in physical requirements, semianalytical analysis for the KEK-LS storage ring reveals that a feedforward scheme with a broadband cavity under Fourier series truncation ($N = 3$) successfully stretches the average bunch length to over 40 ps [3], which fully satisfies the machine's nominal requirements. Crucially, this $N = 3$ truncation baseline corresponds to a relative voltage tracking error ϵ_{rel} of approximately 25%, establishing an operationally acceptable perturbation threshold for bunch lengthening.

Based on this 25% physical tolerance, a moderately band-limited scenario with $N = 6$ is selected as the optimal hardware configuration. Theoretically, the unoptimized Fourier-truncation expansion for $N = 6$ demands a prohibitive peak generator power of approximately 200 kW per cavity. By shifting the operating point to the knee of the GCR-optimized Pareto frontier, the theoretical peak power requirement per cavity can be

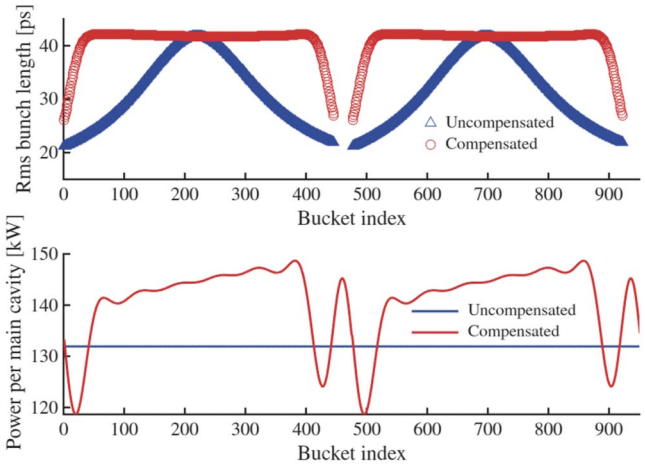


FIG. 6. Rms bunch length (top) and corresponding generator power per main cavity (bottom) across the bucket indices for KEK-LS under two conditions: uncompensated (blue Δ/solid line) and compensated under the $N = 6$ MCF scheme ($\epsilon_{\mathrm{rel}} = 25\%$, red $\circ$/solid line).

reduced to 145 kW, at the cost of a marginal increase in the fitting error ϵ_{rel}. Physically, it is realized by increasing the coupling factor from 3.5 to 4.14 and shifting the cavity detuning frequency from −40.3 kHz to −44.95 kHz.

To further substantiate the optimization benefits, semianalytical simulations are executed based on the calculation framework established in Ref. [3]. It should be noted that this semianalytical model assumes a steady state, inherently neglecting collective bunch instabilities. As illustrated by the calculated power and tracking profiles in Fig. 6, the maximum peak power is 148 kW, slightly exceeding the theoretical value of 145 kW. This discrepancy arises because the theoretical derivation assumes $|\tilde{V}_{g,f,\mathrm{st}}| \gg |\tilde{V}_{g,f,\mathrm{tr}}|$, thereby neglecting the transient component's contribution to the steady-state current $I_{\mathrm{g,st}}$. In practice, however, this omitted transient term slightly elevates the actual peak power requirement. Nevertheless, the resulting average power remains well controlled at approximately 141 kW per cavity. With this MCF compensation implemented, the average bunch length is successfully stretched from the uncompensated 31.1 to 40.9 ps, while the single-cavity peak power increases from 131 to 148 kW. Given that the storage ring utilizes a total of five cavities, the entire rf system requires a peak power increment of approximately 85 kW and an average power scaling of about 50 kW. Compared to a broadband-cavity scheme—which exhibits cavity peak power demand of roughly 50 kW—the proposed MCF scheme achieves comparable bunch-lengthening performance while maintaining a remarkably similar and manageable power overhead, fully validating its feasibility for practical engineering deployment.

B. Application to SSMB: Impact on coherent radiation power

In SSMB light sources, harmonic cavities are employed to stretch the electron bunch length, thereby decreasing the local peak current density and mitigating the damaging IBS effects in the microbunch. However, the high-power EUV radiation scheme relies on coherent echo-enabled modulation, which requires precise spatial-temporal synchronization between the electron bunch and the external seed laser. To maximize laser efficiency, the second-stage modulation laser pulse is designed with an rms length σ_L comparable to the electron bunch length σ_τ. Consequently, any distortion of the longitudinal bunch distribution or deviation relative to the laser pulse severely degrades the interaction overlap, thereby suppressing the resulting coherent radiation power [7].

Assuming a Gaussian temporal envelope for the second-stage laser pulse, the normalized bunching factor $R(\tau)$ within the interaction region is determined by:

$$R(\tau) = \frac{J_{n+1}[a\exp(-\tau^2/2\sigma_L^2)]}{J_{n+1}(a)}, \tag{41}$$

where n is the modulation order and a is the modulation amplitude with the optimal value $a_{\mathrm{opt}} \approx n + 0.81n^{1/3}$.

To account for the effects of centroid shift and bunch-shape distortions, the integrated coherent radiation power W can be evaluated via the generalized overlap integral:

$$W \propto \int_{-\infty}^{\infty} [R(\tau)\cdot\rho_{\mathrm{dist}}(\tau)]^2 d\tau, \tag{42}$$

where $\rho_{\mathrm{dist}}(\tau)$ represents the perturbed longitudinal charge distribution of the electron bunch under TBL effect; both Eqs. (41) and (42) follow the echo-enabled modulation formalism of Ref. [7]. As a baseline, previous simplified analyses that overlooked bunch-shape variations indicated that a bunch centroid shift of less than 20 ps is required to sustain at least 95% of the output radiation power [7].

To evaluate the capability of the proposed transient-compensation framework under these strict synchronization constraints, a systematic case study is conducted based on a typical SSMB storage ring design. The principal machine specifications and the double-rf configurations are summarized in Tables III and IV, respectively.

Following the identical evaluation methodology established in the previous section, we perform a dedicated multiobjective Pareto frontier scan specifically for the SSMB storage ring configuration by continuously varying the weighting ratio C. This calculation independently maps the global trade-off between the tracking precision and the peak generator power overhead under the specific SSMB parameter space. Adopting the operationally acceptable

TABLE III. Principal parameters of the SSMB.

Parameter	Symbol	Value
Nominal beam energy	E_0	600 MeV
Stored beam current	I_0	1 A
Radio frequency (fundamental)	f_{rf}	500 MHz
Harmonic number	h_0	1000
Synchrotron radiation loss per turn	U_0	330 keV
Main rf voltage	$V_{c,f}$	1.2 MV
Natural relative energy spread (rms)	σ_e	1.3×10^{-3}
Momentum compaction factor	α_c	1×10^{-3}
Filling pattern	$\cdots$	$5 \times (175b + 25e)$
Modulation order	n	76

TABLE IV. Principal parameters of the double-rf system for the SSMB.

		Main rf	Harmonic rf
Parameter	Symbol	$(n = 1)$	$(n = 3)$
Rf voltage	$V_{c,n}$	1.2 MV	384.57 kV
Synchronous phase	$n\phi_n$	1.178 rad	-1.5709 rad
Tuning angle	ψ_n	-0.962 rad	1.5707 rad
Total R/Q	R_n/Q	262.5 Ω	20 Ω
Unloaded Q factor	Q_0	40 000	1×10^8

error threshold of $\epsilon_{\mathrm{rel}} = 40\%$, the newly synthesized optimization frontiers are illustrated in Fig. 7.

Operating at this selected $N = 3$ configuration limits the required rf low-level hardware bandwidth to approximately 7.5 MHz. From an engineering perspective, accommodating these high-frequency corrective harmonics inevitably requires a larger transient voltage overhead,

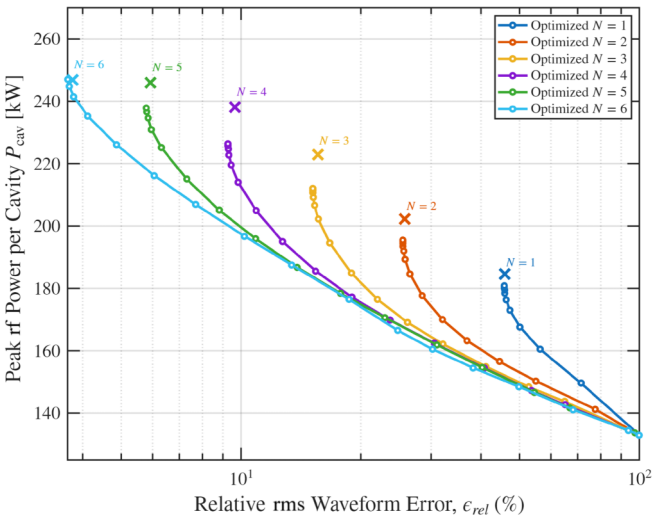


FIG. 7. Multiobjective Pareto frontier scan of the peak generator power versus the residual tracking error for the SSMB storage ring configuration.

TABLE V. Optimized rf parameters for the SSMB double-rf system.

		Main rf	Harmonic rf
Parameter	Symbol	$(n = 1)$	$(n = 3)$
Loaded quality factor	$Q_{L,n}$	5871	1×10^8
Cavity detuning amount	$\Delta f_{\mathrm{res},n}$	-105.09 kHz	55.425 kHz

thereby increasing the peak single-cavity generator power from the uncompensated baseline of 133 to 155 kW. The corresponding self-consistent cavity detuning frequencies and optimized loaded quality factors for this specific operating point are detailed in Table V.

To definitively validate the macroparticle stability and synchronization performance under this GCR-optimized MCF scheme ($N = 3$), high-fidelity turn-by-turn tracking simulations are conducted using the graphics processing unit-accelerated code `STABLE` [24]. `STABLE` provides a self-consistent macroparticle tracking framework that fully incorporates longitudinal beam evolution alongside realistic collective effects.

Figure 8 illustrates the simulated steady-state beam parameters along the train, providing a direct visual benchmark between the uncompensated and regulated scenarios. As shown in the uncompensated case, the TBL effect causes the synchronous phase error to accumulate severely along the bunch train. This induces a massive bunch centroid shift spanning from 60 ps at the train head to -60 ps at the tail.

In sharp contrast, when the GCR-optimized MCF compensation scheme is enabled, the longitudinal bunch length is noticeably lengthened and stabilized at approximately 78 ps, while the overall bunch centroid offset is substantially suppressed. The residual phase deviations observed at the very head and tail of the bunch train stem inherently from the rounding off of the band-limited voltage waveforms, which structurally introduces these localized boundary errors. The peak single-cavity generator power of the main rf system increases from the uncompensated baseline of 133 to 158 kW, representing a peak power increment of approximately 25 kW per cavity, with the average power demand settling at around 147 kW.

By substituting the simulated macroparticle distributions into the analytical formulas in Eqs. (41) and (42), the calculated performance shows that the proposed feedforward compensation scheme boosts the normalized average coherent radiation power from a degraded 78% to a superior 97%. This effectively satisfies the operational requirements and successfully averts the degradation of coherent emission efficiency otherwise caused by severe TBL effects. It demonstrates that the joint MCF scheme can achieve excellent TBL mitigation at an acceptable cost in additional generator power.

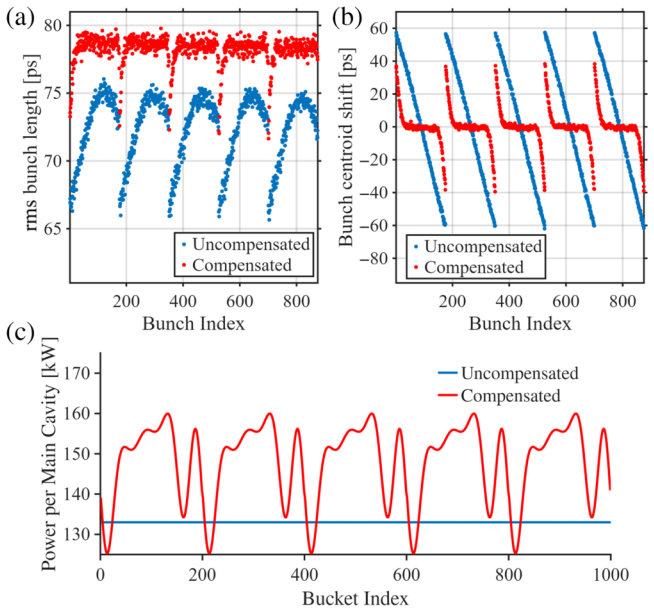


FIG. 8. Steady-state longitudinal beam parameters and rf power profiles across the SSMB bucket indices, comparing cases with and without the GCR-optimized MCF scheme ($N = 3$). The subplots show (a) the rms bunch length σ_τ, (b) the bunch centroid shift $\langle\tau\rangle$, and (c) the required generator power per main rf cavity.

VI. DISCUSSION

A. Stability constraints and modified optimal conditions

The optimal detuning frequency $\Delta\omega_{f,\mathrm{opt}}$ and loaded quality factor $Q_{L,\mathrm{opt}}$ derived in the preceding sections are determined strictly from the objective of minimizing the forward rf generator power. However, in practical storage ring operations, improper combinations of large detuning angles and high loaded quality factors can easily trigger longitudinal coupled-bunch instabilities driven by the fundamental mode impedance of both the main and harmonic cavities. If the coherent instability growth rate exceeds the natural longitudinal radiation damping rate (τ_δ^{-1}), it will inevitably lead to emittance growth or beam loss. Therefore, the unconstrained power-optimum parameters must be systematically evaluated and bounded within a rigorously defined stability envelope.

To efficiently map out the longitudinal stability threshold without resorting to computationally intensive turn-by-turn macroparticle tracking simulations, we employ the semianalytical code Algorithms for Longitudinal Multibunch Beam Stability (`ALBuMS`) [25]. Through this rapid numerical evaluation, a two-dimensional (2D) stable operating region can be accurately mapped out in the $(\Delta\omega_f, Q_L)$ parameter space.

Directly searching for a global multiobjective optimum within this 2D stable domain is computationally intensive. To streamline the optimization process, we propose a dimension-reduction strategy that leverages the analytical dependency defined in Eq. (26). Since this relation mathematically defines an optimal trajectory in the $(\Delta\omega_f, Q_L)$ plane where the forward rf power is minimized for any given Q_L, the feasible search space can be restricted from the entire 2D domain onto this 1D theoretical curve. Consequently, Q_L is treated as the sole independent optimization variable. By evaluating the collective stability margins along this analytical trajectory, the modified optimal quality factor $Q_{L,\mathrm{mod}}$ is uniquely determined at the boundary intersection where the trajectory enters the `ALBuMS`-defined stable region. This approach guarantees that the rf system operates at the absolute minimum possible generator power while strictly satisfying the rigid constraints of longitudinal beam stability.

Once the modified quality factor $Q_{L,\mathrm{mod}}$ is pinned under the stability constraints, the corresponding constrained optimal detuning frequency $\Delta\omega_{f,\mathrm{mod}}$ is inherently fixed by the theoretical trajectory. Substituting these bounded optimal parameters back into the power formulation, the practical minimum forward rf power requirement for the main-cavity feedforward scheme is formalized as:

$$P_{\mathrm{opt}} = \frac{1}{8\sin^2\phi_f}\left(\frac{R}{Q}\right)_f \frac{Q_0 Q_{L,\mathrm{mod}}}{Q_0 - Q_{L,\mathrm{mod}}} \times \left[\left(I_{\mathrm{st}} + I_c\frac{Q_0}{Q_{L,\mathrm{mod}}}\right)^2 + I_{\mathrm{tr}}^2\right]. \tag{43}$$

Consequently, operating under these stability-enforced restrictions introduces an unavoidable power penalty, requiring a higher forward generator power compared to the theoretical unconstrained optimum. The exact magnitude of this overhead is highly sensitive to the specific ring lattice and cavity-design parameters. Nevertheless, this power penalty can be effectively mitigated during the hardware design phase by strategically co-optimizing the harmonic-cavity parameters, thereby reshaping the fundamental impedance profile to allow the main cavity to safely access the desired $Q_{L,\mathrm{mod}}$ and $\Delta\omega_{f,\mathrm{mod}}$ combinations.

To quantitatively evaluate this effect, a parametric stability scan is performed based on the KEK-LS configuration. As illustrated in Fig. 9, the unconstrained power-optimum loaded quality factor is determined to be approximately 7780, which corresponds to the minimum single-cavity power of 145 kW. When Q_L is intentionally shifted to 6000 or 10 000 to satisfy the longitudinal stability margins, the required peak forward power per cavity increases only marginally to around 150 kW. Concurrently, the absolute variation in the detuning frequency is confined to approximately 5 kHz, relative to the optimum operating point. This numerical result explicitly demonstrates that the forward power demand exhibits a remarkable insensitivity to Q_L variations around the Pareto

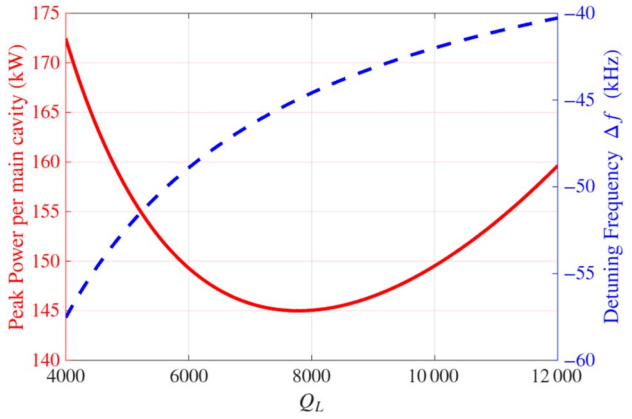


FIG. 9. Peak power requirement per main cavity (red solid line) and detuning frequency $\Delta f = f_{\mathrm{res}} - f_{\mathrm{rf}}$ (blue dashed line) as functions of the loaded quality factor Q_L.

knee, thereby providing a comfortable operational margin for instability mitigation.

B. Comparison with the broadband compensation cavity scheme

To comprehensively evaluate the advantages of the proposed MCF scheme, it is instructive to benchmark its performance against the BCF approach [9]. The BCF scheme introduces an additional, dedicated low-Q cavity into the storage ring specifically to counteract voltage transients. By lowering the quality factor, the cavity bandwidth is intrinsically broadened, allowing for rapid transient voltage adjustments with minimal reactive power demand.

To establish a rigorous comparison, we extend our proposed optimization framework to analyze the BCF scheme and derive its theoretical optimal design formulas. We assume that the broadband cavity is tuned to operate in a purely resistive mode by setting its detuning frequency to zero ($\Delta\omega_c = 0$). Its primary objective is to generate an exact counteracting voltage waveform $V_{b,\mathrm{tr}}$. For the beam-passage duration ($0 < \tau \leq n_t t_b$), the required compensation voltage is expressed as:

$$\tilde{V}_{g,c}(\tau) = \left(\frac{R}{Q}\right)_{\mathrm{tot}} I_0 \frac{n_g}{n_t}\omega_{\mathrm{rf}}\tau + V_{g,c,\mathrm{dc}}, \tag{44}$$

and during the gap interval ($n_t t_b < \tau \leq (n_t + n_g)t_b$):

$$\tilde{V}_{g,c}(\tau) = -\left(\frac{R}{Q}\right)_{\mathrm{tot}} I_0 \omega_{\mathrm{rf}}\tau + V_{g,c,\mathrm{dc}}, \tag{45}$$

where $(R/Q)_{\mathrm{tot}} = F_f(R/Q)_f + hF_h(R/Q)_h + \frac{\omega_c}{\omega_{\mathrm{rf}}}(R/Q)_c$ represents the weighted total longitudinal impedance of the accelerator ring and ω_c is the resonant angular frequency of the broadband cavity.

According to the beam-cavity interaction equations, the required generator driving current for the BCF is governed by:

$$\tilde{I}_{g,c}(t) = \frac{1}{\omega_c(R/Q)_c}\frac{d\tilde{V}_{g,c}}{dt} + \frac{1}{2Q_{L,c}(R/Q)_c}\tilde{V}_{g,c}(t). \tag{46}$$

To minimize the peak transmitter power, we optimize the dc voltage pedestal ($V_{g,c,\mathrm{dc}}$) to balance the current demands at the boundaries of the bunch train, enforcing the minimax criterion: $|\tilde{I}_{g,c,\max}| = |\tilde{I}_{g,c,\min}|$. By substituting these balanced boundary conditions into the power formulation $P_{g,c} = \frac{1}{2}R_{L,c}|\tilde{I}_{g,c}|^2$ and optimizing with respect to the loaded quality factor, we obtain the ideal optimal loaded quality factor for the BCF, in agreement with the earlier optimization at KEK [9]:

$$Q_{L,\mathrm{opt}} = \frac{n_g n_t \pi}{n_g + n_t}\frac{\omega_c}{\omega_{\mathrm{rf}}}. \tag{47}$$

The corresponding ideal minimum required power for the BCF under perfect triangular compensation is given by:

$$P_{\mathrm{opt}} = \frac{1}{2}\frac{(R/Q)^2_{\mathrm{tot}}}{(R/Q)_c} I_0^2 \frac{\omega_{\mathrm{rf}}}{\omega_c}\frac{n_g(n_t + n_g)}{n_t}\pi. \tag{48}$$

However, for a practical system constrained by a finite amplifier bandwidth N, the ideal linear slope is replaced by a truncated Fourier series. Applying our GCR methodology, the voltage-derivative ripples are characterized by the extremum factors $k_{\max}(N)$ and $k_{\min}(N)$. Consequently, the localized increase in the peak power demand adjusts the optimal loaded Q and minimum power requirement to:

$$Q_{L,\mathrm{opt}}(N) = \frac{n_g n_t \pi}{(n_g + n_t)(k_{\max}(N) - k_{\min}(N))}\frac{\omega_c}{\omega_{\mathrm{rf}}}, \tag{49}$$

$$P_{\mathrm{opt}}(N) = P_{\mathrm{opt}} \cdot (k_{\max}(N) - k_{\min}(N)). \tag{50}$$

This formulation allows for a precise determination of the amplifier bandwidth required to maintain potential-well stability within a specified power budget, utilizing the exact same objective function $\mathcal{J}(\mathbf{c})$ as defined for the MCF scheme. To establish a realistic benchmark, the nominal hardware parameters for the broadband cavity are adopted from the practical KEK prototype design [9], as summarized in Table VI.

To systematically evaluate the impact, we generate the Pareto frontiers for both configurations under the KEK-LS baseline parameters (Table I), mapping the fundamental trade-off between the required generator peak power and the relative voltage fitting error ϵ_{rel}, as illustrated in Fig. 10.

TABLE VI. Principal parameters of the dedicated BCF system assumed for the benchmark comparison.

Parameter	Symbol	Value
Resonant frequency	f_c	1.5 GHz
Unloaded quality factor	Q_0	17937
Loaded quality factor	Q_L	292
Total characteristic impedance	R/Q	60 Ω

The optimization frontiers reveal profound physical insights and critical engineering implications regarding spectral coordination. Evidently, under standard unoptimized Fourier series truncation, the MCF scheme suffers from an inflated peak power demand that vastly exceeds the BCF baseline. This discrepancy stems from the fundamental bandwidth limitations of high-Q cavities; forcing such structures to trace sharp gap discontinuities via rigid frequency clipping inherently triggers severe gibbs-induced derivative overshoots, penalizing the system with immense transient reactive power. Conversely, the BCF scheme leverages its inherently wider bandwidth (low-Q) to execute swift voltage transitions free from high-frequency ringing, naturally yielding a more favorable Pareto frontier with lower power demands.

Crucially, the optimization curves reveal that when the GCR method is applied, increasing the truncation order N enables the MCF Pareto frontiers to achieve a performance slope nearly identical to that of the BCF approach. Specifically, at a representative configuration of $N = 6$, the MCF scheme constrains the error ϵ_{rel} to a window of 10% to 20%, effectively bridging the performance gap and approaching the BCF baseline. This enhancement originates from the GCR-driven edge round-off effect, which strategically smooths the boundary transitions and curtails the transient power spikes. This numerical evidence underscores that scaling up the active harmonic channels (N) within the MCF framework, paired with GCR optimization, provides a highly effective and power-efficient feedforward compensation capability.

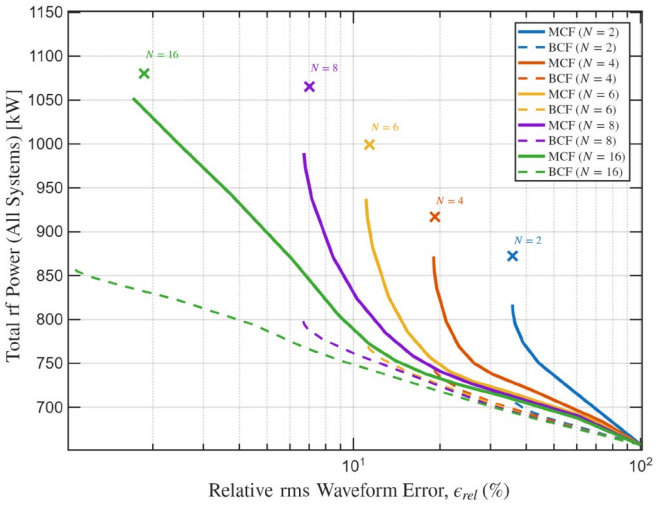


FIG. 10. Pareto optimization frontiers mapping the single-cavity peak rf power requirements against the relative voltage tracking error ϵ_{rel}, comparing the MCF and BCF schemes for KEK-LS parameters.

This optimization demonstrates that the MCF strategy can achieve TBL compensation performance comparable to that of a broadband cavity, without requiring any additional hardware. Consequently, the engineering complexities, physical straight-section space allocation, and vacuum or cryogenic infrastructures inherent to a dedicated kicker cavity system can be avoided. The GCR-optimized MCF framework thus offers a useful solution that significantly improves the cost-effectiveness and flexibility of TBL mitigation in modern storage rings.

C. Dependence on duty factor and train-repetition frequency

The total rf power demands of the MCF and BCF schemes are analyzed as functions of the duty factor $d = n_t/(n_t + n_g)$ and the train-repetition frequency $f_{\mathrm{train}} = 1/[(n_t + n_g)t_b]$. The calculations are performed with the modulation bandwidth of the rf system fixed at 3.3 MHz, using the KEK-LS parameters of Tables I and II as the baseline. The filling pattern is taken as a single bunch train of $n_t + n_g = 119$, 238, 476, or 952 buckets at fixed bucket spacing, corresponding to train-repetition frequencies from $8f_0$ down to f_0, where f_0 is the revolution frequency of the ring.

Figure 11 shows the resulting total rf power as a function of d. In both schemes, the power demand increases rapidly as d decreases, since a larger gap fraction produces a stronger transient to compensate. Remarkably, the MCF power curves for all four bunch-train-repetition frequencies collapse onto a single curve. The BCF power, in contrast, increases at fixed duty factor as the repetition frequency decreases and approaches the MCF curve only at large duty factors.

The high-Q_L narrow band main cavity of the MCF acts as an integrator: the generator current is governed by the time derivative of the compensation voltage rather than by its amplitude, as expressed by Eq. (35), where the peak current is set by the slope factor $S_0 = \omega_{\mathrm{rf}}(R/Q)_{\mathrm{tot}}I_0$ and the derivative factors $k_{\max} = n_g/n_t$ and $k_{\min} = -1$, both pure ratios of bucket numbers that depend only on the duty factor. Although the peak-to-peak amplitude $A = (R/Q)_{\mathrm{tot}}I_0\omega_{\mathrm{rf}}n_g t_b$ grows linearly with the gap duration, its time derivative does not: changing the train-repetition frequency at fixed duty factor only stretches the triangular waveform in time, and the required generator current, and with it the power, remains unchanged. The repetition frequency enters the MCF solely through the modulation bandwidth Nf_{train}.

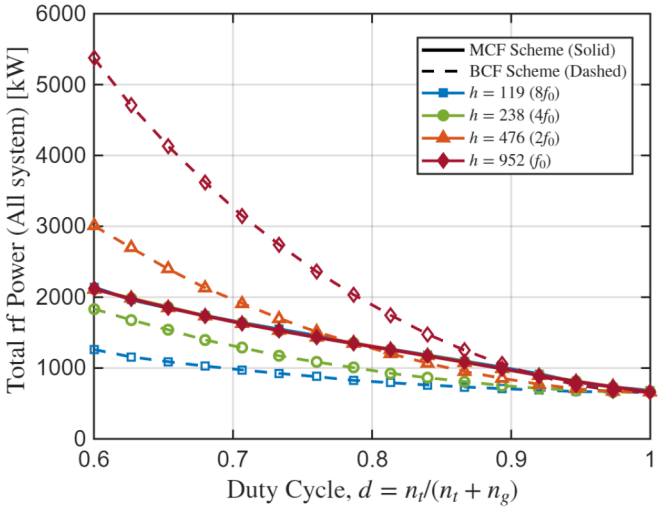


FIG. 11. Comparison of total required rf power between the proposed MCF scheme (solid curves with solid markers) and the BCF scheme (dashed curves with open markers) as a function of bunch-train duty cycle $d = n_t/(n_t + n_g)$ for various train-repetition frequencies f_{train} (parameterized by total bucket number per train period $n_t + n_g \in \{119, 238, 476, 952\}$, corresponding to $8f_0$ down to f_0).

The broadband cavity of the BCF, in contrast, is operated at a low Q_L to obtain its bandwidth; the low Q_L entails a small shunt impedance and a filling time shorter than the transient duration, so the cavity cannot integrate the drive and its generator must sustain the full amplitude of the compensation voltage rather than its derivative. The power demand therefore follows the voltage amplitude, which grows linearly with the gap duration $n_g t_b$: according to Eq. (48), the filling-pattern dependence is the factor $n_g(n_t + n_g)/n_t$, which scales linearly with the train length (or inversely with the train-repetition frequency) at fixed duty factor. These scalings separate the application domains of the two schemes: filling patterns with long gaps and low train-repetition frequencies favor the MCF, whose power demand is insensitive to the gap length, whereas patterns of many short trains at high repetition frequencies favor the BCF, whose power penalty remains small.

D. Robustness to imperfect filling patterns

The analysis so far assumes an ideal filling pattern with identical bunch charges. In operation, the pattern is imperfect on two distinct time scales: bunch-to-bunch charge noise within the train and a slow evolution of the pattern itself, driven by the position-dependent Touschek lifetime that results from the nonuniform bunch lengthening along the train and by the uniform decay of the stored current.

Bunch-to-bunch charge fluctuations occupy high-frequency spectral components far beyond the modulation bandwidth Nf_{train} of the correction: the MCF waveform synthesizes only the first N train harmonics of the fill envelope, and the GILD slope on which the correction is based depends only on the slowly varying averages I_0 and d.

The slow drifts, in contrast, are decoupled from the correction by their time scales: they occur over minutes to hours, many orders of magnitude slower than both the correction period and the LLrf loop bandwidth. The feedforward waveform table can be refreshed periodically from the measured fill pattern (adaptive feedforward), while the residual slow errors are absorbed by the standard low-bandwidth amplitude and phase feedback loops of the rf system, the same loops that already maintain the harmonic-cavity voltage as the beam current decays. A fully quantitative assessment under realistic noisy fills is left for future experimental study.

VII. CONCLUSION

In this paper, we have developed a novel and cost-effective main-cavity feedforward scheme to mitigate the TBL effect in dual-frequency rf systems. As the theoretical foundation of this framework, the GILD model has been established to decompose the TBL voltage into steady-state and transient components. Based on the GILD model, a rigorous parameter analysis for power minimization was conducted, specifically incorporating band-limited constraints into the evaluation. This parameter optimization revealed that Fourier truncation inherently triggers gibbs-induced overshoots at the bunch-train boundaries, counterproductively inflating the peak power demand. To circumvent this fundamental bottleneck, the parametric analysis was advanced into a global wave-reconstruction approach, culminating in the development of the GCR optimization method. By actively resynthesizing and optimizing the spectral coefficients of the driving waveform within an allowable fitting tolerance, the GCR method successfully dampens the high-frequency derivative spikes, smoothing the sharp boundary transitions and strictly clipping the peak generator power demand.

The efficacy and universality of this MCF and optimization framework have been thoroughly validated across two distinct machine scenarios via self-consistent multiparticle tracking simulations. For the KEK-LS storage ring, where bunch lengthening and Touschek lifetime are the primary objectives, operating near the knee region of the Pareto frontier with a moderate 6-MHz bandwidth optimizes the peak power per main cavity to 148 kW, successfully restoring the average bunch length from 31.1 to 40.9 ps. Meanwhile, for the SSMB light source where phase-space fidelity is paramount, expanding the bandwidth to $N = 3$ (7.5 MHz) manages the peak generator power at 158 kW, which tightly locks the bunch centroids along the train within the strict synchronization threshold

and boosts the normalized average coherent radiation power from 78% to 97%.

Because the power-optimal main-cavity parameters may excite longitudinal coupled-bunch instabilities, the loaded quality factor (Q_L) and detuning frequency (Δf) must be optimized with collective stability taken into account, and the cavity parameters may deviate from the theoretically optimal power conditions to avoid instability zones. We propose a robust main-cavity parameter design methodology tailored for instability avoidance, demonstrating that the impact of adjusting the quality factor on the peak power requirement remains well within an acceptable engineering margin. Benchmark comparisons with the BCF approach demonstrate that the GCR-optimized MCF strategy achieves comparable TBL compensation performance within a practical power budget. Consequently, the engineering complexities, physical straight-section space allocation, and vacuum or cryogenic infrastructures inherent to developing a dedicated broadband auxiliary cavity can be entirely bypassed. The proposed framework establishes an elegant, software-driven retroactive solution that maximizes the utility of existing rf assets, offering a promising technological pathway for the design and optimization of next-generation light sources.

ACKNOWLEDGMENTS

The authors thank Dr. Tianlong He from the University of Science and Technology of China for reviewing the manuscript and providing valuable comments. This work is supported by the National Key R&D Program of China (Grant No. 2022YFA1603401).

DATA AVAILABILITY

There are no publicly available research data or software supporting this manuscript. Requests for further information or data should be sent to the authors.

[1] J. M. Byrd and M. Georgsson, Lifetime increase using passive harmonic cavities in synchrotron light sources, Phys. Rev. ST Accel. Beams **4**, 030701 (2001).

[2] P. F. Tavares, A. Andersson, A. Hansson, and J. Breunlin, Equilibrium bunch density distribution with passive harmonic cavities in a storage ring, Phys. Rev. ST Accel. Beams **17**, 064401 (2014).

[3] N. Yamamoto, T. Takahashi, and S. Sakanaka, Reduction and compensation of the transient beam loading effect in a double rf system of synchrotron light sources, Phys. Rev. Accel. Beams **21**, 012001 (2018).

[4] T. He, W. Li, Z. Bai, and L. Wang, Longitudinal equilibrium density distribution of arbitrary filled bunches in presence of a passive harmonic cavity and the short range wakefield, Phys. Rev. Accel. Beams **24**, 044401 (2021).

[5] J. M. Byrd, S. De Santis, J. Jacob, and V. Serriere, Transient beam loading effects in harmonic rf systems for light sources, Phys. Rev. ST Accel. Beams **5**, 092001 (2002).

[6] G. Penco and M. Svandrlik, Experimental studies on transient beam loading effects in the presence of a superconducting third harmonic cavity, Phys. Rev. ST Accel. Beams **9**, 044401 (2006).

[7] P. Fang *et al.*, Picosecond bunch-centroid stabilization in SSMB storage rings via low-R/Q harmonic cavities and GILD-based feedforward compensation, in *Proceedings of the 17th International Particle Accelerator Conference, IPAC'26, Deauville, France, 2026* (JACoW, Geneva, 2026), pp. 4930–4933.

[8] R. Warnock and M. Venturini, Equilibrium of an arbitrary bunch train in presence of a passive harmonic cavity: Solution through coupled Haïssinski equations, Phys. Rev. Accel. Beams **23**, 064403 (2020).

[9] D. Naito, N. Yamamoto, T. Takahashi, T. Yamaguchi, and S. Sakanaka, Design and low-power measurement of the broadband kicker cavity used to compensate the transient beam-loading effect in synchrotron light sources, Phys. Rev. Accel. Beams **28**, 112002 (2025).

[10] N. Yamamoto and A. Gamelin, Bunch-lengthening RF system using active normal-conducting cavities, in *Proceedings of the 67th ICFA Advanced Beam Dynamics Workshop on Future Light Sources, FLS2023, Lucerne, Switzerland, 2023* (JACoW, Geneva, 2023).

[11] N. Yamamoto, T. Takahashi, and S. Sakanaka, Beam loading compensation for optimal bunch lengthening with harmonic cavities, in *Proceedings of the ICFA mini-Workshop on Mitigation of Coherent Beam Instabilities in Particle Accelerators (MCBI 2019), Zermatt, Switzerland, 2019*, CERN Yellow Reports: Conference Proceedings Vol. 9 (CERN, Geneva, 2019), p. 96.

[12] N. Yamamoto and S. Sakanaka, Feasibility study of an active harmonic cavity for bunch lengthening in an electron storage ring, in *Proceedings of the 19th Annual Meeting of Particle Accelerator Society of Japan (PASJ2022), Online, 2022* (Particle Accelerator Society of Japan, Tsukuba, 2022), p. 698.

[13] F. Perez *et al.*, Active harmonic EU cavity: Commissioning and operation with beam, Nucl. Instrum. Methods Phys. Res., Sect. A **1072**, 170195 (2025).

[14] H. Shaker, Harmonic EU cavity commissioning operation and TBL compensation, in *Proceedings of the ESLS RF & HarmonLIP Workshops 2025* (ALBA Synchrotron, Cerdanyola del Vallès, Spain, 2025).

[15] M. Ruprecht, Influence of transient beam loading on the longitudinal beam dynamics at BESSY VSR, *Proceedings of the 6th International Particle Accelerator Conference, IPAC'15, Richmond, VA, USA, 2015* (JACoW, Geneva, 2015).

[16] T. He, Novel perturbation method for judging the stability of longitudinal beam dynamics, Phys. Rev. Accel. Beams **25**, 094402 (2022).

[17] J. Tückmantel, Cavity-beam-transmitter interaction formula collection with derivation, CERN, Tech. Rep. ATS-Note-2011-002, 2011.

[18] H. Damerau, Beam loading, in *CERN Accelerator School on RF for Accelerators* (2023).

[19] D. Boussard, RF power requirements for a high intensity proton collider, in *CERN Accelerator School on RF Engineering for Particle Accelerators, Oxford, England* (CERN, Geneva, 1992) (CERN-92-03).

[20] B. E. Karlsen-Baeck, T. Argyropoulos, A. Butterworth, R. Calaga, I. Karpov, H. Timko, and M. Zampetakis, Effects of cavity pre-detuning on RF power transients at injection into the LHC, J. Instrum. **19**, P04018 (2024).

[21] E. Hewitt and R. E. Hewitt, The Gibbs–Wilbraham phenomenon: An episode in fourier analysis, Arch. Hist. Exact Sci. **21**, 129 (1979).

[22] P. T. Boggs and J. W. Tolle, Sequential quadratic programming, Acta Numer. **4**, 1 (1995).

[23] J. Nocedal and S. J. Wright, *Numerical Optimization*, 2nd ed. (Springer, New York, 2006).

[24] T. He and Z. Bai, Graphics-processing-unit-accelerated simulation for longitudinal beam dynamics of arbitrary bunch trains in electron storage rings, Phys. Rev. Accel. Beams **24**, 104401 (2021).

[25] A. Gamelin, V. Gubaidulin, M. B. Alves, and T. Olsson, Semianalytical algorithms to study longitudinal beam instabilities in double rf systems, Phys. Rev. Accel. Beams **28**, 054401 (2025).